Measurements of turbulent crossflow separation created by a curved body of revolution

P. A. GREGORY[1]†, P. N. JOUBERT[2] AND M. S. CHONG[2]

[1]Maritime Platforms Division, DSTO, Fishermans Bend, Victoria, 3067, Australia
[2]Department of Mechanical and Manufacturing Engineering, University of Melbourne,
Parkville, Victoria, 3010, Australia

Using the method pioneered by Gurzhienko (1934), the crossflow separation produced by a body of revolution in a steady turn is examined using a stationary deformed body placed in a wind tunnel. The body of revolution was deformed about a radius equal to three times the body's length. Surface pressure and skin-friction measurements revealed regions of separated flow occurring over the rear of the model. Extensive surface flow visualization showed the presence of separated flow bounded by a separation and reattachment line. This region of separated flow began just beyond the midpoint of the length of the body, which was consistent with the skin-friction data. Extensive turbulence measurements were performed at four cross-sections through the wake including two stations located beyond the length of the model. These measurements revealed the location of the off-body vortex, the levels of turbulent kinetic energy within the shear layer producing the off-body vorticity and the large values of $\langle uw \rangle$ stress within the wake. Velocity spectra measurements taken at several points in the wake show evidence of the inertial sublayer. Finally, surface flow topologies and outer-flow topologies are suggested based on the results of the surface flow visualization.

1. Introduction

The flow over a slender body of revolution undergoing a steady turn may create a pair of off-body vortices if the local angle of incidence is large enough to create crossflow separation. These off-body vortices that are created by this three-dimensional flow separation are large turbulent flow structures that have a significant effect on the forces exerted by the fluid on the body. When examining the specific case of a submarine in a steady turn, these vortices create large amounts of hydro-acoustic noise, as well as producing regions of unsteady flow which may affect propeller performance.

The investigation of the crossflow separation produced by bodies of revolution at incidence to the free stream has usually been confined to a steady examination of the body at constant pitch. A large body of research investigating the flow over prolate spheroids has been conducted at Virginia Polytechnic Institute and State University. This includes the work of Ahn (1992), Chesnakas & Simpson (1994, 1996, 1997), Goody *et al.* (1998) and Wetzel, Simpson & Chesnakas (1998), who recorded boundary layer and wake measurements using both laser Doppler anemometry and

† Present address: Renault F1 Team Limited, Enstone, Oxfordshire, UK.
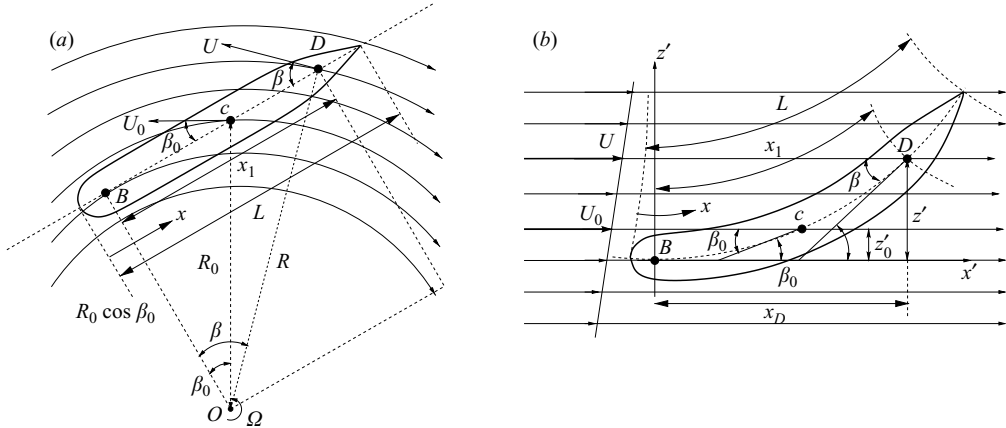
FIGURE 1. Body of revolution turning about point O (*a*), with the equivalent deformed body which preserves the change in the local angle of attack (*b*).

hot-wire methods, in addition to surface flow measurements. More recent experiments featured the use of a dynamic model mount such as that used by Hoang, Wetzel & Simpson (1994) to measure surface pressure measurements on the prolate spheroid in a time-dependent manoeuvre. Wetzel & Simpson (1998) continued their earlier separation studies on the 6:1 prolate spheroid by extending their research to include unsteady skin-friction measurements obtained using this dynamic apparatus. All wake measurements conducted in these studies were limited to axial locations lying within the length of the body.

In contrast to the flow over a body of revolution at incidence, the flow over a body of revolution in a steady turn creates a variation in the local angle of attack along the length of the body. Flow measurements from a body of revolution in a steady turn are more difficult to obtain, mainly due to experimental problems associated with rotating-arm apparatus. Measurements of the crossflow separation caused by the flow over a body of revolution in a steady turn have been limited in the open literature to the work conducted by Lloyd & Campbell (1986), who measured vorticity magnitude within the wake for a variety of turn radii.

1.1. *The use of curved bodies*

In this investigation, the method of Gurzhienko (1934) was used to replicate the flow created by a body moving in a steady turn. This method creates a deformed body that, when placed in rectilinear flow, preserves the same change in angle of attack which is created along a straight body in a steady turn. Figure 1 shows the relationship between a straight body turning about point O with angular velocity Ω and the equivalent deformed body placed in rectilinear flow.

Clearly, the local angle of incidence varies along the centreline of the straight body in a steady turn. At a point B, the local angle of incidence is equal to zero. This location is referred to as the 'pivot point' in naval architecture. As the centroid of the body c rotates at a distance R_0 about point O, the local angle of incidence at c is equal to β_0, while the local value of velocity is equal to U_0. At an arbitrary point D, the local angle of incidence is equal to β while the local value of velocity is equal to U. The length of the body between the two arbitrary points B and D is equal to x_1.

x/L	d/D
0.79	1.00
0.82	0.97
0.86	0.84
0.88	0.74
0.90	0.63
0.92	0.51
0.94	0.39
1.00	0.00

TABLE 1. Coordinates of the tapered tail.

Gurzhienko (1934) showed that the equation of the centreline of the body is equal to

$$z' = R_0 \cos \beta_0 \left[\cosh \left(\frac{x'}{R_0 \cos \beta_0} \right) - 1 \right], \qquad (1.1)$$

while the equations which define the deformed cross-sections passing through an arbitrary point D are given by

$$z' = x_1 \left[\cosh \left(\frac{x' - x_D}{x_1} - \operatorname{arcsinh} \frac{1}{n x_1} \right) \right] - \frac{1}{n}, \qquad (1.2)$$

where $n = R_0 \cos \beta_0$. A body whose centreline is deformed according to (1.1) will have the same change in local angle of attack β along its centreline as the straight body undergoing a steady turn with radius R_0.

Gurzhienko's methods were used by Chang & Purtell (1986) to provide an experimental validation for a numerical method to predict the forces on a turning body and to examine the flow separation created by this body. Their experimental program recorded surface pressures and skin-friction measurements, although their wake measurements were limited to a single plane of mean velocity measurements recorded at $x/L = 0.94$.

This investigation is the first time that extensive turbulence measurements have been recorded within the separated flow over a curved body. The experimental apparatus used also made it possible to record measurements of the wake beyond the body.

2. Experimental techniques

All experiments were conducted in the large closed circuit wind tunnel at the University of Melbourne. The octagonal working section measures 5 ft 6 in. × 4 ft 3 in. × 17 ft long (1.68 × 1.30 × 5.18 m). The working section is constructed from longitudinal bars of aluminium, which are bolted onto the uprights of the wind tunnel. These strips are mounted a small distance away from each other creating a 'slotted wall' wind tunnel, designed to minimize wall interference. All results were taken with a free-stream velocity U_∞ in the working section of approximately 15 m s^{-1}, which gave $Re = 10^6$ per metre and $Re = 2.58 \times 10^6$ based on model length.

2.1. Bodies of revolution

Two bodies of revolution were constructed with identical profiles. The models were 2.58 m long and 0.26 m in diameter, giving an L/D ratio of 9.9. They featured a hemispherical nose, a long straight middle section and a gently tapered tail. The coordinates of the tail section are given in table 1. Each model comprised two
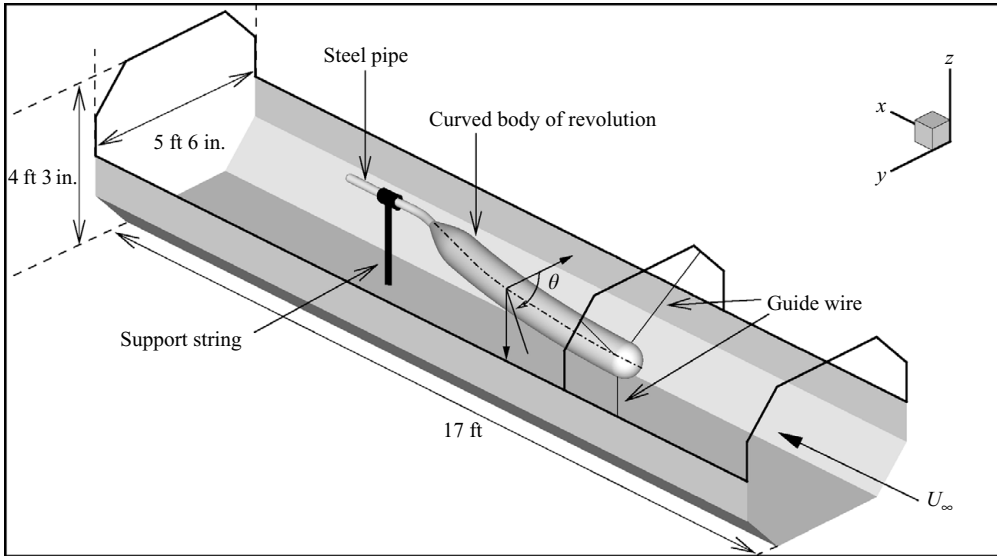
FIGURE 2. Schematic of the curved body of revolution mounted in the University of Melbourne wind tunnel. The upper walls of the working section are removed for clarity. The orientation of the variable θ used to plot C_p and C_f values at cross-sections along the body is also shown. $\theta = 0°$ corresponds to the outboard side of the body (the contracted side of the body), which faces the free stream. $\theta = 180°$ corresponds to the inboard side of the body (the elongated side). $\theta = 90°$ corresponds to locations below the centreline of the body.

symmetrical fibreglass shells which were bolted onto a subframe made from four aluminium disks which provided internal support. These disks in turn were bolted onto a steel pipe of diameter 60.3 mm, which ran along the length of the model. The steel pipe was then clamped to a vertical sting which held the model in place using a cantilever arrangement. Three steel support wires 2 mm in diameter were then mounted onto the front aluminium disk to provide extra support. The arrangement of the experimental apparatus is shown in figure 2.

The first model tested was a straight body used to check various experimental apparatus. These included checks for flow symmetry, assessing the effects of the wire supports on the flow, as well as checking the effectiveness of the turbulence stimulators within the boundary layer. The straight body was also used to calculate the accuracy of the Preston tubes used to record skin-friction measurements. The turbulence stimulators were small disks 0.012 in. in diameter with a height of 0.008 in., uniformly spaced at 0.05 in. intervals. They were placed on the body at $x/L = 0.05$.

Several boundary layer profiles were taken along the straight body at station # 9 ($x/L = 0.25$) and station # 15 ($x/L = 0.48$) to quantify the effect of the support wires. These profiles showed that the presence of the wire created an increase in C_f of the order of 25 % within 5° of the wires. The C_f measurements for the curved body were recorded on the lower surface of the body, where only one guide wire was present (see figure 2), so for the results shown later in § 3.2, this increase in C_f is limited to the region of $85° \leqslant \theta \leqslant 95°$. Velocity profiles taken along the length of the support wires showed that the wake disturbance was limited to $U/U_\infty = 0.95$ close to the surface of the body, where a 3-inch fairing was used. Beyond the fairing, the bare wire caused a maximum wake velocity deficit of $U/U_\infty = 0.93$ at $x/L = 0.25$, which decreased to

Mean flow		Turbulent flow	
term	uncertainty	term	uncertainty
ρ	$0.012\,\mathrm{kg\,m^{-3}}$	$\langle U \rangle$	$0.29\,\mathrm{m\,s^{-1}}$
U_∞	$0.03\,\mathrm{m\,s^{-1}}$	$\langle V \rangle, \langle W \rangle$	$0.28\,\mathrm{m\,s^{-1}}$
C_p	0.026	k	$7\,\%$
$C_f \times 10^3$	0.14		

TABLE 2. Summary of experimental uncertainty values.

$U/U_\infty = 0.95$ at $x/L = 0.48$. The wake behind the outer section of the wire was seen not to spread significantly.

The second body of revolution was deformed about a radius of 7.749 m, i.e. $R_0 = 3L$, which is representative of the tightest turn possible for such a body performing a rudder-induced turn. The value of β_0 was chosen to be 8.71°, which located the pivot point at $x/L = 0.0$. This is typical for a body in a tight turn. For reasons of manufacture, it was decided not to deform this model about the hyperbolic curve given by (1.1). Instead, a circular arc was used. This made it easier for the model-makers to build the moulds for the fibreglass shells, as well as making it far easier to bend the steel pipe section used as the central support sting. For our particular choice of R_0 and β_0, the difference between a circular arc and the exact hyperbolic curve is less than 1.2 %.

2.2. *Turbulence measurements*

Turbulence data were recorded using a crossed hot-wire probe, capable of recording two components of velocity simultaneously. Construction of the wires used 5-μm- and 3-μm-diameter platinum-core Wollaston wire soldered to a DANTEC 22P51 crossed-wire probe.

Calibration of the wire was carried out using the dynamic method outlined in Perry (1982, p.70–80). Calibration errors were limited to within $\pm 0.5\,\%$ for mean velocity measurements, although persistent calibration errors of up to 2 % were found at low values of mean x-component velocity $\langle U \rangle$. These larger errors existed for $\langle U \rangle / U_\infty < 0.2$. Errors between the measured and analytical Reynolds stresses were limited to $\pm 2.0\,\%$.

Crossed wires are able to measure two components of velocity simultaneously, either along the $x-y$ plane ('uv' mode) or the $x-z$ plane ('uw' mode). Thus all measurements had to be repeated to record the three components of velocity at any given measurement point.

The temperature within the working section of the wind tunnel was able to be maintained to within $\pm 0.5\,°\mathrm{C}$ of the calibration temperature, by venting the air within the laboratory to the outside atmosphere via a large cargo door.

Spectra measurements were made using uncalibrated matched cross-wires and the raw voltage measurements were sampled. The cutoff frequency used was 10 kHz. Butterworth filters were used to low-pass filter the signals at 0.4 times the sampling frequency of 25 kHz. Measurements were taken with 100 bursts of 2^{18} samples.

2.3. *Uncertainty estimates*

The uncertainty estimates for the mean and turbulent flow measurements are summarized in table 2. Note that the uncertainty value for skin friction was obtained on the straight body of revolution. The uncertainty estimates given for the turbulent

flow quantities are representative of the worst value of calibration error, which was present at low velocities. They do not take into account the errors caused by using a cross-wire in a turbulent, three-dimensional flow. These errors are discussed separately in §4.1.

2.4. *Flow visualization*

Surface flow visualization was carried out using a mixture of kaolin powder in kerosene. Aeolic acid was also used to assist in the wetting of the powder within the kerosene. The mixture was applied to the body with a large brush whilst the tunnel was running at operational speed. Photos were taken after a settling time of one hour. Two sorts of flow visualization tests were performed. Initially, entire sections of the model were painted with the kerosene mixture. This gave an overall picture of the surface flow. Later, small areas upstream of regions of interest were painted and portions of the mixture were allowed to be swept along the body's surface. In this way, individual streamline patterns were obtained. Flow visualization photographs were taken with the body mounted inside the wind tunnel, as well as with the upper section of the body removed from the wind tunnel and mounted against a backing sheet.

3. Surface flow

Measurements of surface pressure coefficient C_p were recorded at 24 axial stations along the body. Measurements of C_f were recorded at eight stations along the body, with a clustering of measurements at the tail of the body.

3.1. *Pressure measurements*

Figure 3 shows plots of C_p for selected stations along the curved body. Only stations where both surface pressure and skin-friction measurements were obtained are shown in this figure. From $x/L = 0.39$ onwards, the crossflow component of velocity is large enough to produce C_p plots at each cross-section which resemble that of a cylinder in crossflow. The minimum C_p value occurs close to $\theta = 90°$, which is the centreline of the body. With increasing streamwise distance, the C_p values begin to 'flatten' for $\theta > 135°$. This trend becomes noticeable at $x/L = 0.67$ and beyond. At $x/L = 0.80$, the C_p data exhibit a second inflection, or turning point. This turning point is initially located at $\theta = 135°$ at $x/L = 0.80$ and it occurs for smaller values of θ (i.e. moves closer to the centreline) with increasing streamwise distance. At $x/L = 0.91$ the C_p values can be regarded as 'flat' for $\theta > 90°$. As mentioned in Wetzel *et al.* (1998), examination of C_p values can qualitatively show regions of massive flow separation, but they are a poor guide to determining the exact separation location. Clearly, the flow can be regarded as separated at $x/L = 0.91$, but more information is required to identify the location of the separation point.

3.2. *Skin-friction measurements*

Measurements of skin friction were taken on the curved model using Preston tubes, which were connected to static pressure tappings at various locations along the body. Velocity profiles taken along the straight body of revolution showed that these tubes gave values of C_f to within $\pm 5\%$ of the value calculated using the Clauser Chart method for an attached boundary layer.

It was found during the experiment that the reading from the Preston tube was quite sensitive to its direction relative to the longitudinal axis of the wind tunnel. With the complex three-dimensional flow occurring over the surface of the curved
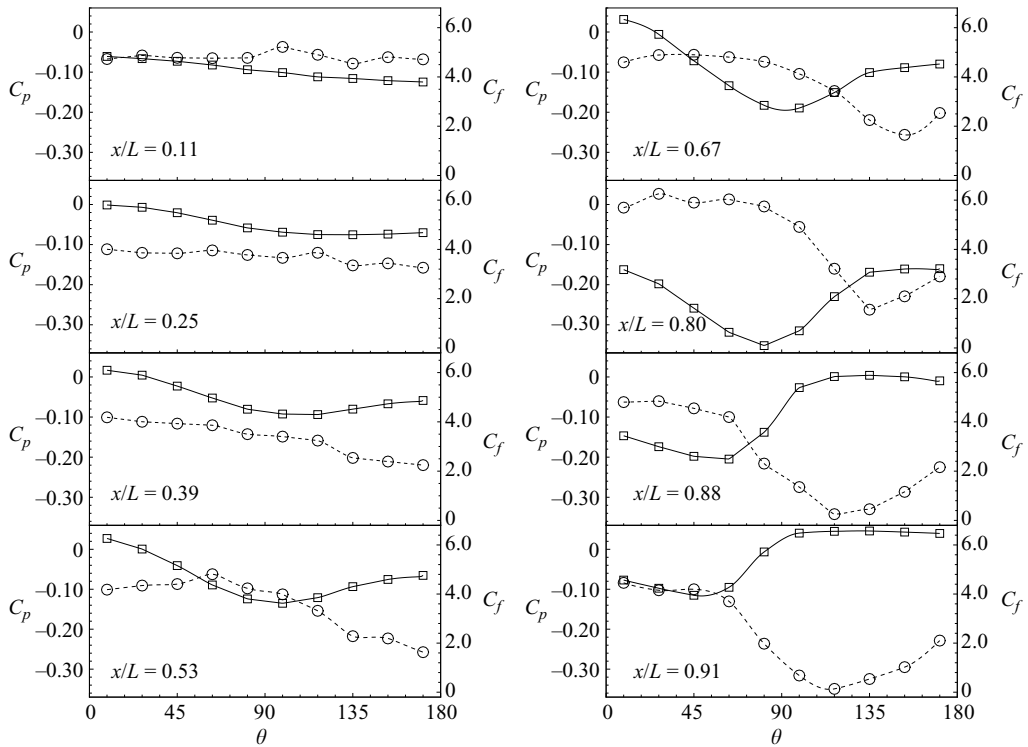
FIGURE 3. Plots of C_p and $C_f \times 10^3$ versus θ at various cross-sections along the curved body: —□—, C_p; – –○– –, C_f.

body, care had to be taken to ensure that the Preston tube was aligned correctly with the local flow direction. It was also necessary that the tubes were placed flush with the surface of the body, which was not a straightforward task considering the local curvature of the body and the length of the tubes (which was equal to 20.0 mm). The uncertainty estimate of C_f supplied in table 2 is representative of inconsistencies created by two factors. Firstly, variability in the surface finish at the mouth of the Preston tube, and secondly, variability in the fit between the curved surface of the body and the Preston tube itself. Ensuring the Preston tube lay flush with the body was essential in order to obtain consistent readings.

Estimates of the additional uncertainty created by the potential mis-alignment between the Preston tubes and the mean flow direction were calculated at $x/L = 0.53$. At this station, the tubes were rotated through an angle of 10°, between the curved centreline of the body and the longitudinal axis of the tunnel itself. This change in angle produced differences in measured C_f of between 5 % and 17 % ($\Delta C_f \times 10^3$ of between 0.001 and 0.890). The alignment error of the Preston tubes when aligning them with the mean flow direction was estimated to be 5°.

Preston tubes are designed to give accurate readings of skin friction within a turbulent boundary layer that remains attached. Naturally these readings become invalid within a separated boundary layer, as the scaling laws on which the Preston tube method are based are no longer valid. Additional techniques (such as flow visualization) are required to provide further information in order to determine the location of any separated flow regions.

Plots of C_f at various stations are shown in figure 3. There is a significant amount of scatter in the C_f measurements for small values of x/L, but the values become smoother and more consistent with downstream distance. This scatter was attributed to support wire effects, as well as localized effects from the turbulent stimulators. From $x/L = 0.67$ and beyond, an inflection point and associated C_f minimum is present at $\theta \approx 150°$. Initially, the location of this minimum is very close to the inboard side (or trailing edge). For increasing x/L, the value of θ at the minimum decreases and at $x/L = 0.91$, the location of the C_f minimum is closer to $\theta \approx 120°$.

As discussed in Wetzel *et al.* (1998), the location of a C_f minimum can be viewed as the beginning of three-dimensional crossflow separation. So for regions of the body beyond the location of the C_f minimum, the flow can be considered separated. The movement of the C_f minimum can be viewed in context of the 'flattening' of the C_p values. With increasing x/L, the region of 'flat' C_p values increases in size. The location of the second C_p turning point (the first occurs for $\theta < 90°$, the second for $\theta > 90°$) moves closer to the centreline of the body ($\theta = 90°$). This is consistent with the location of the C_f minimum moving closer to the centreline for increasing x/L. Figure 3 shows how the location of the C_f minimum moves in conjunction with second inflection point on the C_p curve. The behaviour of the C_p and C_f data tells us what is intuitively expected, that the region of separated flow along our curved body increases as x/L increases. As one moves towards the tail of the body, the local angle of attack increases, which produces larger crossflow components of velocity.

The C_f data produced by the Preston tubes are representative of similar data produced by separated flow from bodies of revolution. However, owing to the limitations of the apparatus within the separated flow region, measurements of the C_f minima are a qualitative guide to the flow separation location only, and not an accurate measurement of C_f in this region.

3.3. *Surface flow visualization*

The first flow visualization involved applying the kerosene mixture to the rear third of the body. Photographs were then taken of the body mounted inside the wind tunnel. In these photographs, all background objects (such as the wind tunnel floor) have been removed for clarity. Figures 4(*a*) and 4(*b*) show the visualization results over the rear of the body. The location of the primary separation line is clearly shown as a dark line separating two regions of mixture strength. The region of separated flow is outlined by the white region of mixture, whilst the regions of attached flow are grey in appearance. This is due to the attached flow blowing more mixture along the body, which eventually blows off the body and into the free stream. This effectively dilutes the mixture in these regions.

Since the mixture concentration varies over the body, regions of attached flow dry faster than regions of separated flow, where the boundary layer is stalled.

Mixture placed in regions of separated flow stagnate and sit on the body. These regions take far longer to dry and thus they have a very different appearance. They appear much 'wetter' and thicker when compared to the thinner covering of powder in the regions of attached flow. An oblique view of the separation line is shown in figure 4(*c*). This is a good example of how clearly the mixture is able to define the primary separation line. However, the ability to resolve any reattachment lines is poor, as shown in figure 4(*d*). Some surface lines are visible which separate thicker, white, 'wet'-looking regions from thinner, grey areas. Based on 4(*d*), it would seem that the region of separated flow near the rear of the body (where it meets the support sting) extends to the seam separating the upper and lower surfaces of the body. Also evident
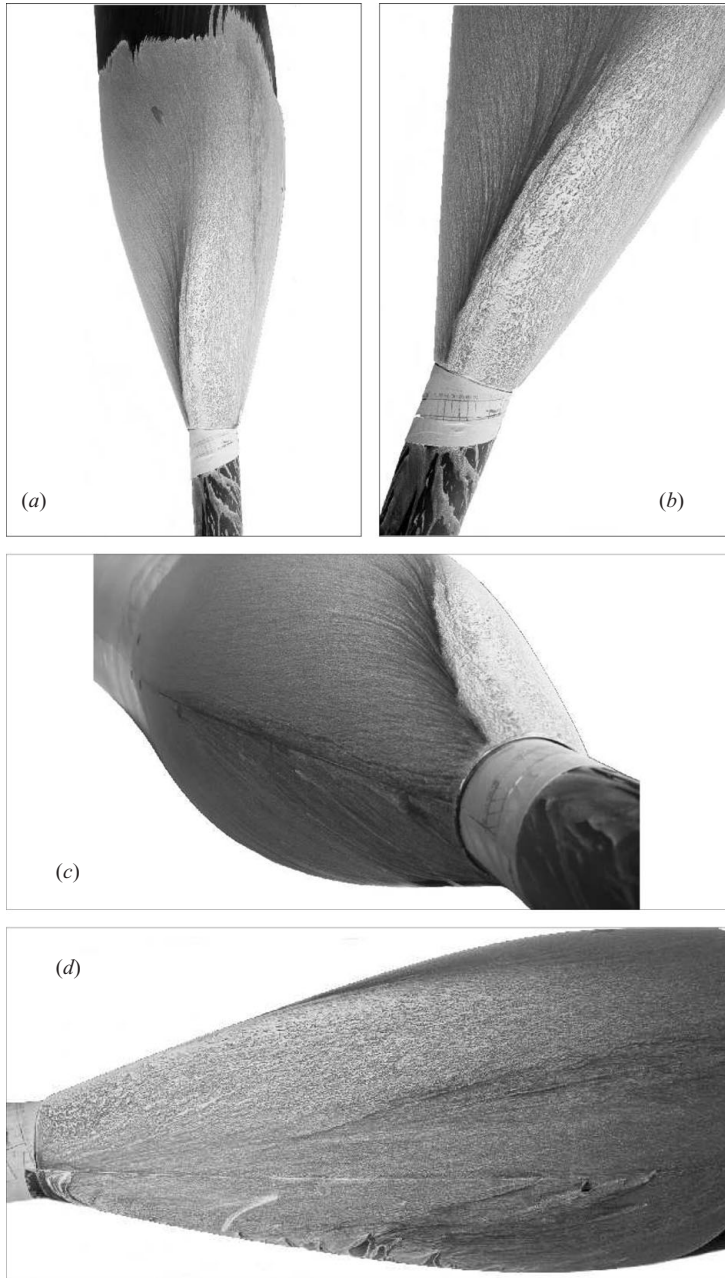
FIGURE 4. Flow visualization over the rear third of the curved body.

is the trend of these lines to droop and drift towards the lower surface of the model. The direction of the mixture near the seam shows that gravitational effects on the mixture in this region are strong.

The effect of gravity was easily seen in a separate set of flow tests in which only a narrow band of mixture was applied along the upper surface, at roughly $x/L = 0.7$. From this band, separate flow streamlines were able to be visualized. These are shown in figure 5.
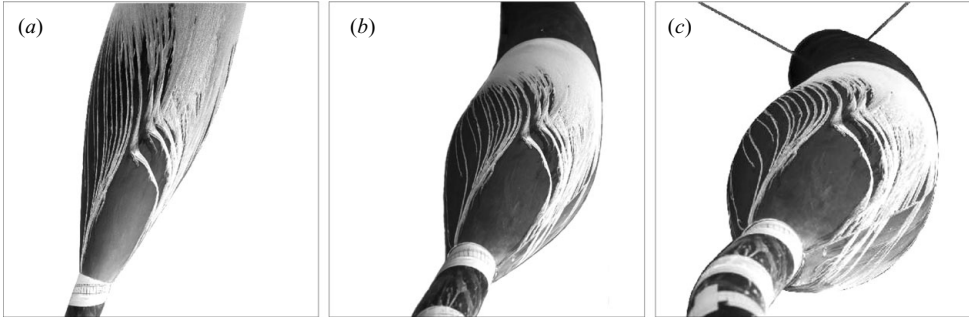
FIGURE 5. Views of the rear third of the curved body with individual streamlines showing gravity effects at the tail of the model.

This figure clearly shows surface streamlines converging into the primary separation line. It also shows the beginning of the separated flow region. Mixture, which is pushed into this area where the boundary layer is stalled, begins to drip slowly across the body due to the force of gravity. These streamlines in the separated flow area are not representative of the flow itself and are an inherent problem of the flow visualization technique. A better view of the 'stalled' mixture dripping across the body and onto the lower surface is shown in figure 5(c).

For the last set of photographs, the entire upper half of the curved body of revolution was painted using the kerosene mixture. Once this mixture had dried, the body of revolution was disassembled and the upper half was removed from the wind tunnel. It was then placed against a backing sheet. This enabled photographs of the surface flow to be taken from any angle, free from any obstructions created by the wind tunnel working section. Photographs of the surface flow against the backing grid are shown in figure 6. These images provide a better picture of the overall length of the separated flow region that occurs along the inboard side of the model.

The side view of the curved body shown in figure 6(b) shows the full extent of the streamwise distance of the region of separated flow. It clearly shows the beginning of flow separation and a long thin region of thick, 'wet' mixture that is situated between the separation and reattachment line. The side view suggests that the flow remains attached below the reattachment line, close to the seam that separates the upper and lower halves of the body. The side view suggests that the flow begins to separate just aft of the bolt holes located at $x/L = 0.54$, which are visible on the far right of figure 6(b). Recall from §3.2 and figure 3 that this is consistent with the C_f measurements taken at $x/L = 0.53$ and $x/L = 0.67$, which suggests that a C_f minimum forms between these two stations. The region of attached flow that lies along the seam of the curved body is also consistent with the C_f measurements taken near $\theta = 180°$, which showed very little change in C_f magnitude from $x/L = 0.39$ onwards.

4. Wake measurements

Velocity and turbulence measurements using a cross-wire were taken at various locations of x/L. The location of each wake measurement plane relative to the body is shown in figure 7. These were taken at right angles to the axis of the tunnel in order to simplify the arrangement of the traversing system mounted on the roof of the wind tunnel. Initially, three sets of measurements were recorded at $x/L = 0.9$, 1.0 and
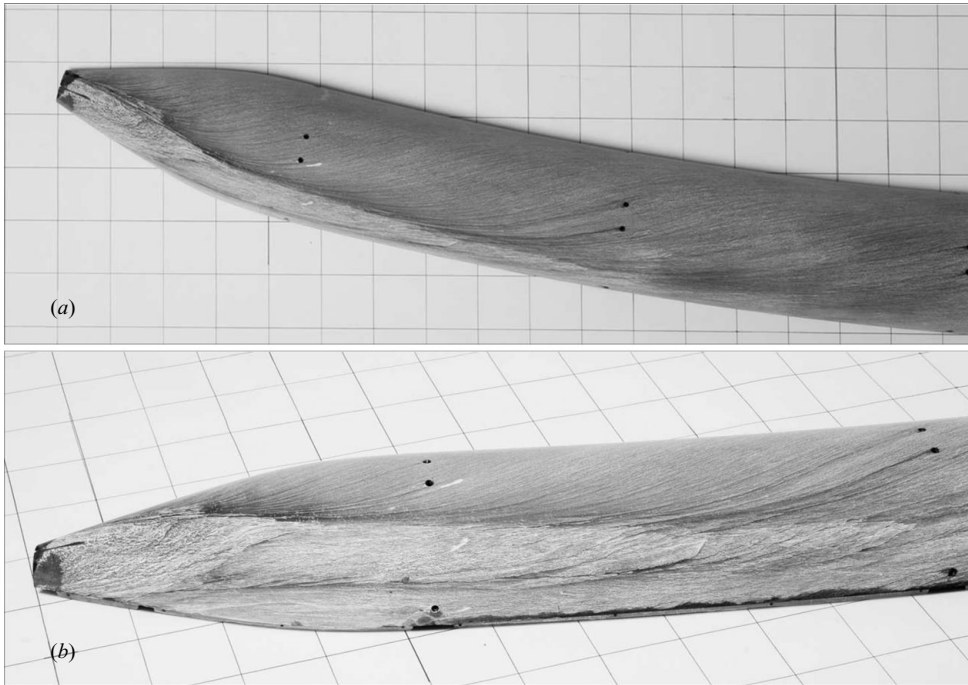
FIGURE 6. Top (*a*) and side views (*b*) of the surface flow features over the curved body of revolution against a backing grid.
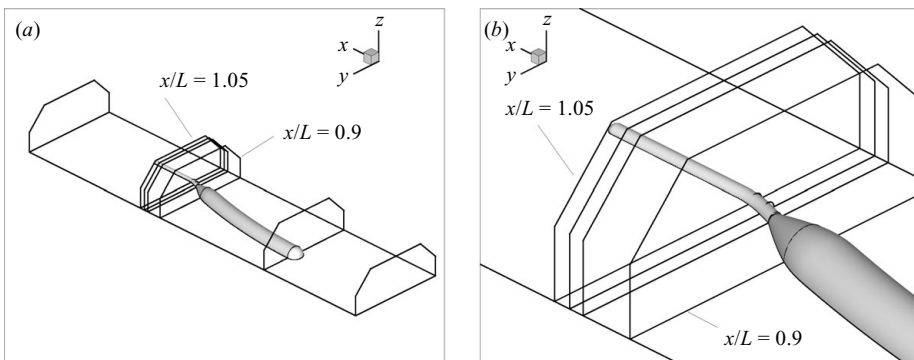
FIGURE 7. Location of wake measurement planes within the working section of the wind tunnel (*a*) and a view of the planes intersecting the body and sting (*b*).

1.05. These measurements all featured an angular resolution of $10°$, with 30 points in the radial direction. The distribution of the measuring points at these locations is shown in figure 8. Once these measurements had been recorded and the location of the off-body vortex had been found, an extra set of measurements was taken at $x/L = 1.05$ for $\theta = 35°$. Additionally, a fourth set of measurements was recorded at $x/L = 1.025$. This plane featured azimuthal stretching to place more points within the core of the vortex.
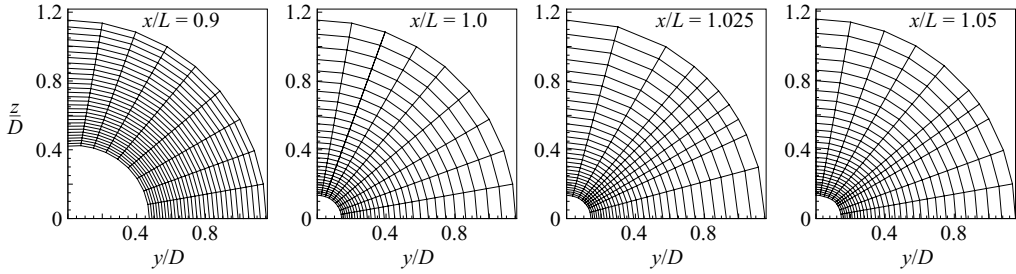
FIGURE 8. Location of data points used for wake measurements at various planes along the curved body.

4.1. *Three-dimensional effects*

Some discrepancies were observed between the measured value of $\langle U \rangle$ depending on the orientation of the cross-wire probe. This was attributed to problems caused by using a cross-wire probe in a region of three-dimensional, highly turbulent flow. Several workers have attempted to quantify the errors created when using cross-wire probes in such flows. Tutu & Chevray (1974) used an analytical method to show that measurement errors for the Reynolds stresses could be as large as 28 % if the turbulence intensity was equal to 35 %. For turbulence intensity levels of 20 % and less, errors in mean velocity and Reynolds stresses were limited to roughly 3 % and 12 % respectively. Such magnitudes are far larger than any errors associated with the calibration process. Experiments recorded by Lim (1985) measured the instantaneous velocity angle and calculated the 'cone angle', which is a measure of the spread of all instantaneous velocity angles. Lim (1985) showed that the error between measured and observed Reynolds stresses was almost zero for a cone angle of 20°, but it rapidly grew to 10 % for a cone angle of 30° and to 20 % for a cone angle of 40°. Although no measurements of cone angle were recorded in this experiment, the value of the mean velocity angle $\langle \theta \rangle$ calculated from the mean velocity field gives an indication of the angle between the mean velocity vector and the cross-wire probe.

The value of $\langle U \rangle$ recorded from the cross-wire was compared with Pitot-static tube measurements of $\langle U \rangle$ at $x/L = 1.0$. These showed that the cross-wire was able to obtain accurate results whilst in 'uw' mode. This also suggests that the effect of the local turbulence intensity on the static pressure measurement obtained with the static tube was negligible. Except for a small region of flow at $x/L = 1.05$, the value of the measured mean velocity angle whilst in 'uw' mode never exceeds 15°. The measured values of the $\langle V \rangle$-component of velocity are larger, which produces greater values of mean velocity angle when the cross-wire is in 'uv' mode. Values of $\langle \theta \rangle$ as high as 40° were recorded in the region close to the y-axis. This places in doubt the ability to measure accurately the $\langle V \rangle$-component of velocity in this region of the wake, as well as the Reynolds stress component $\langle uv \rangle$. Contour plots of mean velocity angle $\langle \theta \rangle$ for $\langle uv \rangle$ measurements are shown in figure 9.

In this figure, contours of the mean velocity angle are plotted with contours of the local intensity level $k/(|U|^2)$. Figure 9 shows that the magnitude of $k/(|U|^2)$ is never larger than 20 %, except at $x/L = 1.0$ in a region close to the sting. This suggests that any errors caused by large turbulence intensities are confined to a region close to the sting. Figure 9 also shows that the region of large velocity angle (i.e. $\langle \theta \rangle > 30°$) is confined to a region close to the y-axis. Any errors created by the large flow angle between the mean velocity vector and cross-wire probe will be located in this
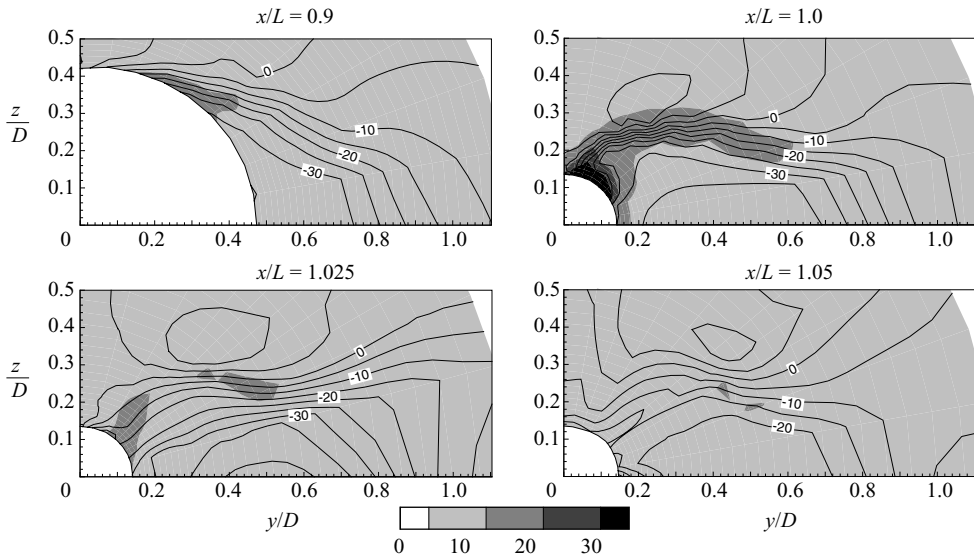
FIGURE 9. Solid contours of $k/(|U|^2)$ at each measurement station. The contour interval is equal to 10%. Contours of mean velocity angle $\langle \theta \rangle$ are overlaid for the uv mode. The contour interval is equal to 5°. Selected contour values are labelled.

region. The areas of large flow angle $\langle \theta \rangle$ have low levels of local turbulence intensity, suggesting that the probability of large cone angles being present in these regions is low. Plots of in-plane streamlines (figure 11) and turbulence measurements (figures 12, 13 and 14) show that these regions lie outside the flow features of interest in this experiment, namely the shear layer and the centre of the off-body vortex.

4.2. *Mean velocity measurements*

Contour plots of $\langle U \rangle$-component velocity measured at the four cross-sections through the wake are shown in figure 10. Sectional streamlines calculated by integrating the measured $\langle V \rangle$- and $\langle W \rangle$-components of velocity are shown in figure 11. Note that the velocity component plotted is that recorded whilst the wire is in 'uw' mode. At $x/L = 0.9$ there is no visible vortex structure.† The data show a region of high-velocity fluid close to the y-axis, near the body. At $x/L = 1.0$ there is evidence of an off-body vortex, with circular sectional streamlines converging to a focal point. At this point, the off-body vortex is being created, although it is still joined to the sectional streamlines which meet the body via a saddle point. The sectional streamlines are skewed, in that the streamlines which define the upper and lower regions of flow near the saddle point are not parallel to the y-axis. Sectional streamlines approaching the sting are also not parallel to the y-axis. It is assumed that the streamlines should become parallel to the y-axis as z approaches zero, as the apparatus is symmetrical about the $x-y$ plane. The experiments also show a region of high-velocity fluid close to the y-axis, located below the off-body vortex.

This region of high-velocity fluid ranges from $0.2 \leqslant y/D \leqslant 0.7$. This is consistent with the surface flow visualization shown in figure 6, which showed that the flow remained attached along the length of the body, close to the plane of symmetry

† The phrase 'vortex structure' is used here simply to describe the 'spiralling' motion. The definition of a vortex is still a highly debated issue and there exist several definitions of a vortex.
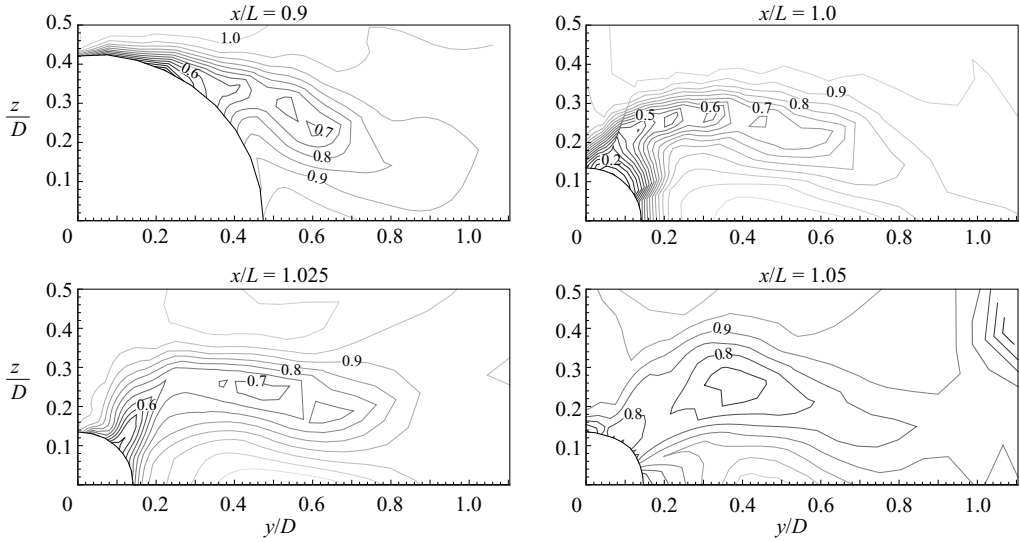
FIGURE 10. Contours of $\langle U \rangle / U_\infty$ at each measurement station. The contour interval for each plot is equal to 0.05. Selected contour values are labelled.
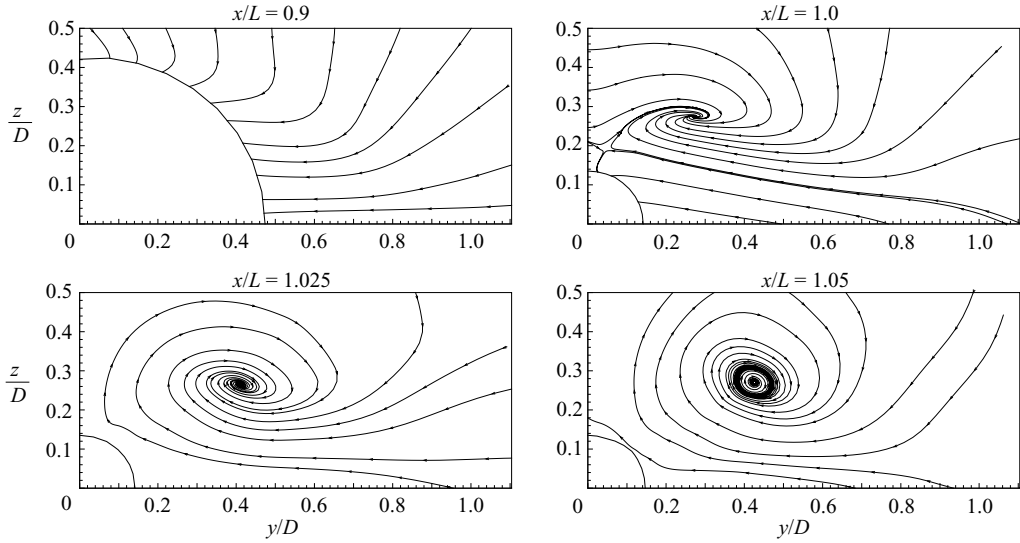
FIGURE 11. Plots of sectional streamlines at each measurement station.

between the upper and lower halves of the body. At $x/L = 1.025$, the data show that a single vortex is present in this region of the wake. As was observed in the previous upstream station, there still exists a large region of high-velocity fluid close to the y-axis, below the off-body vortex. The shape of the wake caused by the defect in $\langle U \rangle$ velocity remains similar to that measured at $x/L = 1.0$. At $x/L = 1.025$, the sectional streamlines below the off-body vortex are almost parallel with the y-axis, yet the 'tilting', or skewness, of the off-body vortex remains. In other words, the major and minor axes of the elliptical focus created by the in-plane velocity field are not aligned with the y- and z-axes. At $x/L = 1.05$ the in-plane vector field now shows the presence of concentric sectional streamlines. The sectional streamlines below the vortex are
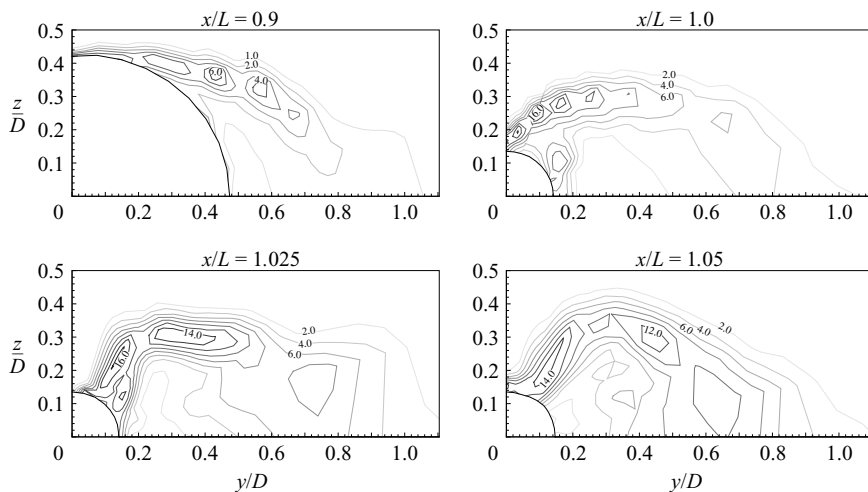
FIGURE 12. Contours of $k/(U_\infty)^2 \times 10^3$ at each measurement station. The contour interval for each plot is equal to 2.0, except at $x/L = 0.9$ where the contour value is equal to 1.0. Selected contour values are labelled.

now parallel to the y-axis. The skewness of the off-body vortex is still present in the results. The shape of the measured wake field remains very similar to that observed at the earlier upstream stations, although the magnitude of the defect has reduced in most areas.

Initially, this skewness of the off-body vortex was attributed to cone angle problems associated with the cross-wire, as the measurements at $x/L = 1.0$ showed large values of $\langle W \rangle$-component velocity in the geometrical plane of symmetry. Further measurements at downstream stations continued to show this skewness of the off-body vortex, but measurements close to the geometrical plane of symmetry at $x/L = 1.0$ and 1.05 produced values of $\langle W \rangle$-component velocity that were more consistent with the geometry of the apparatus. This would suggest that the cross-wire is able to measure accurately the three components of velocity at these stations. From this, it is fairly certain that the observed skewness of the off-body vortex is a real effect and it is not due to errors in the measurement apparatus.

4.3. *Turbulent kinetic energy*

Contour plots of turbulent kinetic energy k are shown in figure 12 at various locations of x/L. At $x/L = 0.9$ the turbulent kinetic energy is contained within a narrow shear layer that originates at the centreline of the body. The magnitude of k reduces as one moves away from the surface of the body and into the wake region. Recall from figure 8 that the resolution at this location was limited to making measurements in the wake only, so detailed measurements of k within the boundary layer were not recorded. At $x/L = 1.0$, the peak values of k occur within the shear layer whose vorticity generates the off-body vortex. The shear layer is now large enough to be resolved by several data points. Large values of k are observed throughout the area surrounding the centre of the off-body vortex. Values of k then diminish with increasing distance along the y-axis. The results at the next downstream station $x/L = 1.025$ show that higher values of k are measured closer to the sting when compared to the previous station. Additionally, higher values of k are observed within the shear layer close to the vortex core. At the final downstream station
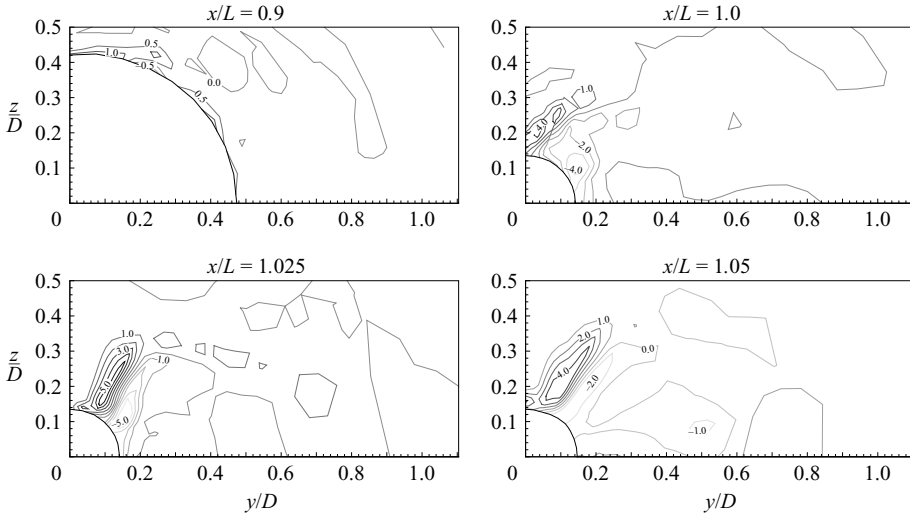
FIGURE 13. Contours of $\langle uv \rangle / (U_\infty)^2 \times 10^3$ at each measurement station. The contour interval for each plot is equal to 1.0, except at $x/L = 0.9$ where the contour value is equal to 0.5. Selected contour values are labelled.

$x/L = 1.05$ the peak levels of k measured within the wake diminish when compared to the previous stations. Higher levels of k are also observed further away from the body, in particular the region close to y/D, $z/D = (0.6, \ 0.0)$.

4.4. Reynolds stresses

Plots of $\langle uv \rangle$ are shown in figure 13. At $x/L = 0.9$, the measurements show very small values of $\langle uv \rangle$ close to the body. As was mentioned with measurements of k at this station (and shown in figure 12), the resolution of the data points at this station is insufficient to resolve satisfactorily any turbulence quantities within the boundary layer. At $x/L = 1.0$, both positive and negative values of $\langle uv \rangle$ exist with positive values on the upper section of the shear layer and negative values on the lower section. This is consistent with the direction of rotation of the off-body vortex. This region of large positive and negative values of $\langle uv \rangle$ located close to the sting, within the shear layer, is still visible at the remaining downstream stations. At $x/L = 1.05$ there exists a small region of negative $\langle uv \rangle$ located near y/D, $z/D = (0.5, 0.1)$ below the centre of the off-body vortex. For other regions of the wake, the values of $\langle uv \rangle$ are very small. The Reynolds stress field continues to be dominated by the regions of positive and negative $\langle uv \rangle$ close to the sting.

Plots of $\langle uw \rangle$ are shown in figure 14. This figure shows that, despite the poor resolution at $x/L = 0.9$, significant levels of negative $\langle uw \rangle$ are measured throughout the shear layer and wake region. A small region of positive $\langle uw \rangle$ stress exists below the shear layer. This Reynolds stress field grows with increasing streamwise distance, as the flow becomes separated and the shear layer produces the vorticity that feeds the off-body vortex. This is particularly evident at $x/L = 1.0$, where large values of negative and positive $\langle uw \rangle$ exist within the shear layer. In contrast to the corresponding plot for $\langle uv \rangle$, negative values of $\langle uw \rangle$ appear above the shear layer, with positive values occurring below. Again, these values are consistent with the clockwise rotation of the off-body vortex. Note that significant levels of both positive and negative $\langle uw \rangle$ are present in the wake, near the centre of the off-body vortex.
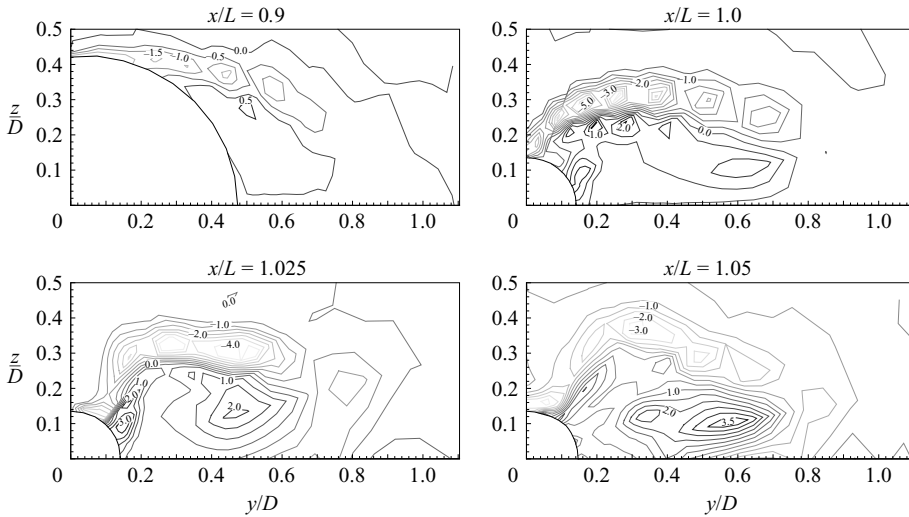
FIGURE 14. Contours of $\langle uw \rangle/(U_\infty)^2 \times 10^3$ at each measurement station. The contour interval for each plot is equal to 0.5. Selected contour values are labelled.
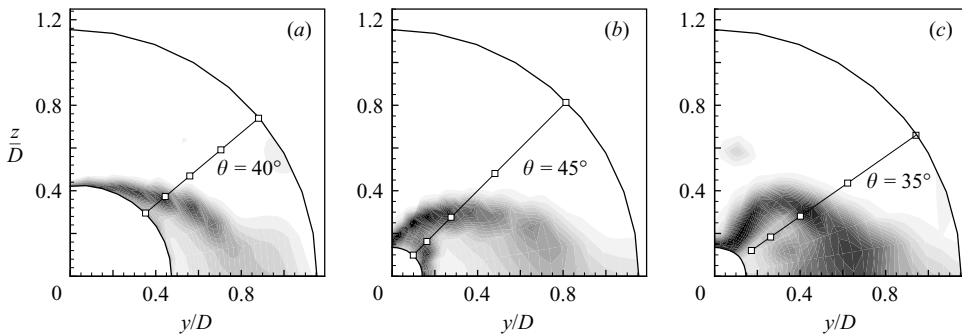
FIGURE 15. Location of data points used for spectra measurements at $x/L = 0.9$ (*a*), $x/L = 1.0$ (*b*) and $x/L = 1.05$ (*c*). Contours of k are shown as a guide to the location of the wake.

In contrast to the measured $\langle uv \rangle$ field, which was found to remain largely constant between $x/L = 1.0$ and $x/L = 1.05$, the measured $\langle uw \rangle$ field evolves with increasing streamwise distance. Large, negative values of $\langle uw \rangle$ are continually produced by the shear layer. At $x/L = 1.05$ these large negative values of $\langle uw \rangle$ are present from the surface of the sting, all the way towards the centre of the vortex. Also noticeable at $x/L = 1.05$ is a large region of positive $\langle uw \rangle$ stress, situated below the centre of the off-body vortex.

4.5. *Velocity spectra*

Spectra measurements were taken at stations $x/L = 0.9$, 1.0 and 1.05. At each station, measurements were taken at five points within the wake along a line of constant θ. The line was chosen to pass through the centre of the off-body vortex at $x/L = 1.0$ and 1.05. The location of the measurement points at each station is shown in figure 15 and table 3. Velocity spectra recorded at the three stations are shown in figure 16. At $x/L = 0.9$, the first three radial locations ($r/D = 0.46$, 0.58 and 0.73) show some evidence of Kolmogorov's hypothesis that energy scales with $\kappa^{-5/3}$ in the inertial subrange. This is most apparent for the spectra Φ_{11} which correspond to the energy

Station		$x/L = 0.9$	1.0	1.05
θ		40	45	35
r/D	1	0.46	0.14	0.21
	2	0.58	0.23	0.32
	3	0.73	0.39	0.49
	4	0.92	0.68	0.76
	5	1.15	1.15	1.15

TABLE 3. Location of spectral measurement points.

spectra for the u-component of velocity. The spectra for the v- and w-components (Φ_{22} and Φ_{33} respectively) fail to match consistently the slope of the $\kappa^{-5/3}$ line. At the fourth location ($r/D = 0.92$) the probe is far enough out of the wake that there is no turbulent energy cascade.

Spectra taken at the first radial location ($r/D = 0.14$) at $x/L = 1.0$ show more evidence of the inertial subrange, with the u- and w-component spectra consistently showing a slope equal to the $\kappa^{-5/3}$ line. At the third radial location ($r/D = 0.39$), all three components of the spectra show evidence of the $\kappa^{-5/3}$ law. As with the previous station, the fourth station lies outside the wake and shows no evidence of a turbulent energy cascade.

Spectra recorded at the final downstream location at $x/L = 1.05$ show that only the u-component spectra agree with the $\kappa^{-5/3}$ law. At this station, the v- and w-component spectra show no evidence of the $\kappa^{-5/3}$ law. Rather, the v- and w-component spectra are shown to collapse onto each other. The collapse of the v- and w-component velocity spectra suggested that perhaps the turbulent wake in this region had reached statistical equilibrium. Turbulent theory suggests that

$$\Phi(\kappa)_{22} = \Phi(\kappa)_{33} = \tfrac{4}{3}\Phi(\kappa)_{11}, \qquad (4.1)$$

is valid within the inertial subrange for a high-Reynolds-number flow (from Tennekes & Lumley 1972, §8.4), where the turbulent energy flux is equal to the turbulent dissipation. Figure 17 shows the velocity spectra at $x/L = 1.05$ plotted with the u-component velocity spectra Φ_{11} multiplied by 4/3. If the turbulent wake was close to equilibrium at this point, all the spectra should collapse onto each other. As can be seen in figure 17, this is not the case, as the rescaled spectra $(4/3)\Phi_{11}$ still do not collapse onto the remaining spectra Φ_{22} and Φ_{33}. This suggests that at all locations upstream of $x/L = 1.05$ the wake is probably dominated by production of turbulent kinetic energy, caused by the shear layer and flow separation.

Velocity spectra measurements recorded by Goody *et al.* (1998) show similar behaviour. Goody's wake measurements were of the separated flow along a 6:1 prolate spheroid at incidence, but were limited to $x/L = 0.6$ and 0.772.

The current configuration meant that taking wake measurements beyond $x/L = 1.05$ became problematic owing to the presence of a large clamp around the horizontal support sting. Therefore, further measurements of the evolution of Φ_{ii} with downstream distance were not possible.

5. Discussion and conclusions

An investigation into the application of measuring the crossflow separation created by the curved body of revolution has shown that it differs in several respects when
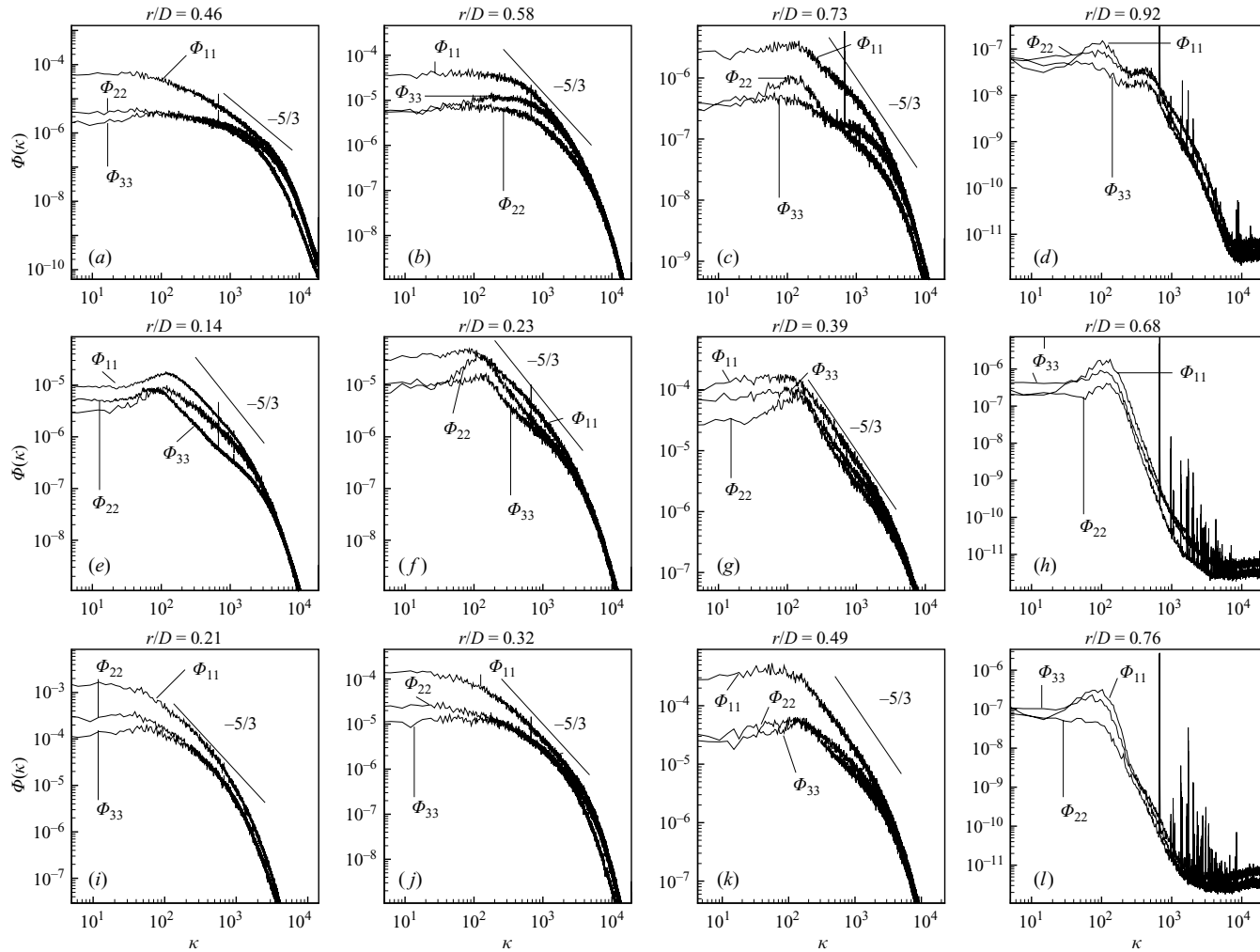
FIGURE 16. Velocity component spectra taken at (a)–(d) $x/L = 0.9$, (e)–(h) $x/L = 1.0$ and (i)–(l) $x/L = 1.05$.
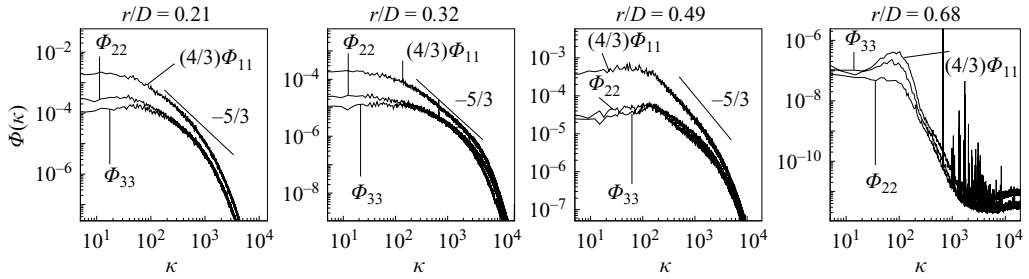
FIGURE 17. Velocity component spectra taken at $x/L = 1.05$ with modified scaling for Φ_{11}.

compared to the separation created by a body placed at constant incidence. One difference is in the shape of the sectional streamline patterns taken just beyond the point of flow separation. Goody *et al.* (1998) measured flow streamlines at $x/L = 0.6$ for a 6:1 prolate spheroid with a mean angle of attack of 10°. They showed that the $\langle V \rangle$-component of velocity was predominantly positive (i.e. streamlines pointing away from the body). In contrast, the sectional streamlines measured for the curved body at $x/L = 0.9$ point towards the body. At this point, the local angle of attack is equal to 18°. While the C_f measurements and surface flow patterns suggest that three-dimensional separation has occurred at this point, the sectional streamlines show no evidence of it.

Another difference is the behaviour of the turbulent kinetic energy within the shear layer at the point of separation. Plots of k at $x/L = 0.6$ and 0.772 for a 6:1 prolate spheroid with an angle of attack of 20° shown in Chesnakas & Simpson (1997) suggest that the peak values of k vary little between these two stations. Contrast this with the behaviour of k for the curved body between $x/L = 0.9$ and $x/L = 1.0$ shown in figure 12. The peak value of k at $x/L = 1.0$ is three times larger than that measured at the previous station, although, as discussed in §4.3, the spatial resolution within the shear layer at $x/L = 0.9$ may not be sufficient to obtain an accurate reading. However, the magnitude of k continues to increase between $x/L = 1.0$ and 1.025. The local angle of attack increases from 17.2° to 18.4° between these two locations. It is presumed that the change in angle of attack along the length of the body, which increases the crossflow component of velocity, helps create this increase in k with increasing x/L.

The results of the surface flow visualizations presented in figures 4, 5 and 6 can be used to plot possible surface streamline patterns. In figure 18, individual surface streamlines are overlaid onto the visualization results shown earlier in figure 6. The visualization results suggest that a separation line begins at roughly $x/L = 0.54$. At this location, a reattachment line is also created.

Such a flow feature is labelled as 'open negative streamsurface bifurcation' according to Hornung & Perry (1984), who note that this type of three-dimensional separation often occurs for flow over slender ellipsoids at incidence. A free sheet originates from the separation line (alternatively known as an open negative bifurcation line) and rolls up into the off-body vortex. The presence of this vortex induces a local velocity field which causes the flow to reattach along the reattachment line (alternatively known as an open positive bifurcation line). Naturally, for the case of our curved body, two such flow features are located above and below the plane of symmetry. In this instance, an open free double bifurcation occurs along the symmetry plane. The combined surface and flow streamline patterns are shown in figure 19.
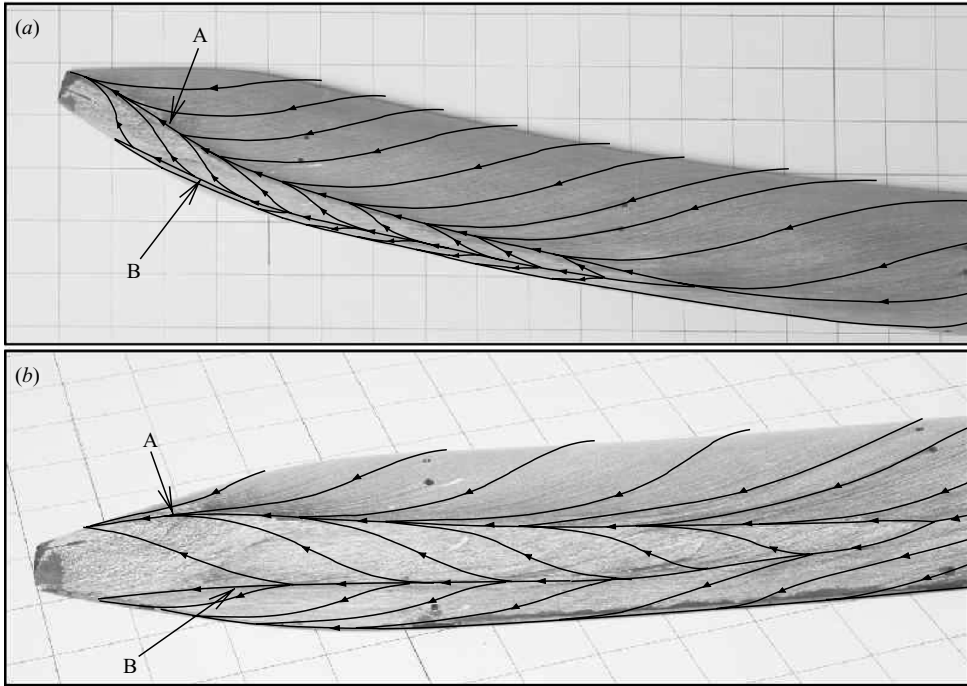
FIGURE 18. Top (*a*) and side view (*b*) of the curved body showing suggested surface streamline patterns overlaid onto the visualization results. The separation line (open negative bifurcation line) is labelled as A, while the reattachment line (open positive bifurcation line) is labelled as B.
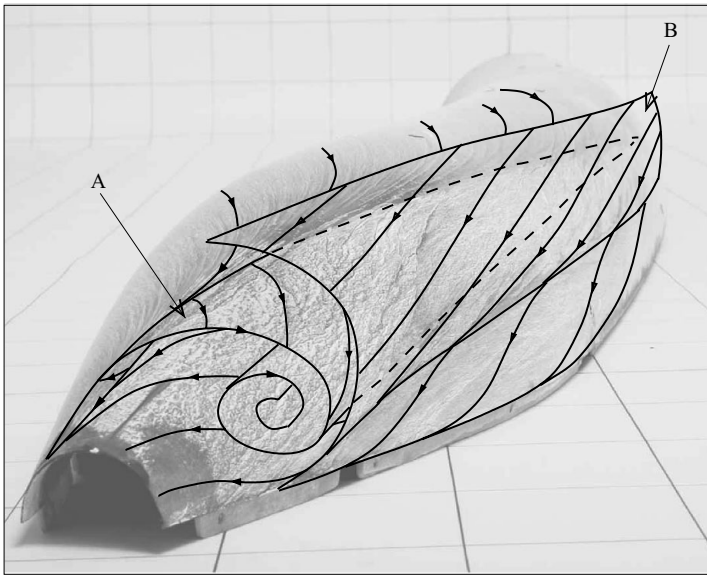
FIGURE 19. Rear view of the curved body showing suggested flow streamlines. The creation of the off-body vortex originates from the separation line (open negative streamsurface bifurcation). The streamsurface which is formed along the bifurcation line is labelled as A. This velocity field creates a streamsurface which reattaches (bifurcates positively) along the reattachment line (open positive bifurcation line). The reattaching streamsurface is labelled as B.

An investigation into the application of the curved body method for investigating the flow over a body of revolution in a steady turn was carried out by the authors and is detailed in Gregory (2006). The conclusions of this thesis showed that the curved body method could accurately replicate the qualitative flow separation behaviour and the production of the off-body vortex. The geometric deformation produced by the method introduced errors in the computation of the forces and moments. The effects of the centrifugal and Coriolis accelerations on the behaviour of the crossflow separation remain a topic for further investigations, as the work of Wetzel & Simpson (1998) shows that, in the instance of an unsteady pitch-up manoeuvre, additional flow acceleration can affect the behaviour of the C_f distribution.

REFERENCES

AHN, S. 1992 An experimental study of flow over a 6 to 1 prolate spheroid at incidence. PhD thesis, Aerospace Engineering Department, Virginia Polytechnic Institute and State University, Blacksburg, VA.

CHANG, M. S. & PURTELL, L. P. 1986 Three-dimensional flow separation and the effect of appendages. In *16th Symposium on Naval Hydrodynamics*, *Berkeley, CA*.

CHESNAKAS, C. J. & SIMPSON, R. L. 1994 Full three-dimensional measurements of the cross-flow separation region of a 6:1 prolate spheroid. *Exp. Fluids* **17**, 68–74.

CHESNAKAS, C. J. & SIMPSON, R. L. 1996 Measurements of the turbulence structure in the vicinity of a 3-D separation. *J. Fluids Engng* **118**, 268–275.

CHESNAKAS, C. J. & SIMPSON, R. L. 1997 Detailed investigation of the three-dimensional separation about a 6:1 prolate spheroid. *AIAA* Journal **35**, 990–999.

GOODY, M., SIMPSON, R. L., ENGEL, M., CHESNAKAS, C. & DEVENPORT, W. 1998 Mean velocity and pressure and velocity spectral measurements within a separated flow around a prolate spheroid at incidence. *AIAA Paper* 98-0630.

GREGORY, P. 2006 Flow over a body of revolution in a steady turn. PhD thesis, Department of Mechanical and Manufacturing Engineering, University of Melbourne.

GURZHIENKO, G. A. 1934 Metod iskrivlenykh modelei primenenie ego k izucheniu krivolineinogo poleta vozdushnykh korablie (The method of deformed bodies and its use in the study of curved flights of airships). *Tech. Rep.* 182. Trudy TsAGI, Moscow, translated and reprinted in English as NACA TM 829 and 830, 1937.

HOANG, N. T., WETZEL, T. G. & SIMPSON, R. L. 1994 Surface pressure measurements over a 6:1 prolate spheroid undergoing time-dependent maneuvers. *AIAA Paper* 94-1908.

HORNUNG, H. G. & PERRY, A. E. 1984 Some aspects of three-dimensional separation. Part I. Streamsurface bifurcations. *Z. Flugwiss. Weltraumforsch.* **8**, 77–87.

LIM, K. L. 1985 Wall shear flow. PhD thesis, Department of Mechanical Engineering, University of Melbourne.

LLOYD, A. R. J. M. & CAMPBELL, I. M. C. 1986 Experiments to investigate the vortices shed from a submarine-like body of revolution. In *59th Meeting of the AGARD Fluid Dynamics Symposium*, *Monterey, CA*.

PERRY, A. E. 1982 *Hot-Wire Anemometry*. Clarendon Press.

TENNEKES, H. & LUMLEY, J. L. 1972 *A First Course in Turbulence*. MIT Press.

TUTU, N. K. & CHEVRAY, R. 1974 Cross-wire anemometry in high intensity turbulence. *J. Fluid Mech.* **71**, 785–800.

WETZEL, T. G. & SIMPSON, R. L. 1998 Unsteady crossflow separation location measurements on a maneuvering 6:1 prolate spheroid. *AIAA J.* **36**, 2063–2071.

WETZEL, T. G., SIMPSON, R. L. & CHESNAKAS, C. J. 1998 Measurement of three-dimensional crossflow separation. *AIAA J.* **36**, 557–564.